


Regional maps of rib cortical bone thickness and cross-sectional geometry

Sven A. Holcombe¹  Yun-Seok Kang,² Brian A. Derstine,¹ Stewart C. Wang^{1,3} and Amanda M. Agnew²

¹Morphomics Analysis Group, University of Michigan, Ann Arbor, MI, USA

²Injury Biomechanics Research Center, The Ohio State University, Columbus, OH, USA

³Department of Surgery, University of Michigan, Ann Arbor, MI, USA

Abstract

Here we present detailed regional bone thickness and cross-sectional measurements from full adult ribs using high resolution CT scans processed with a cortical bone mapping technique. Sixth ribs from 33 subjects ranging from 24 to 99 years of age were used to produce average cortical bone thickness maps and to provide average \pm 1SD corridors for expected cross-section properties (cross-sectional areas and inertial moments) as a function of rib length. Results obtained from CT data were validated at specific rib locations using direct measurements from cut sections. Individual thickness measurements from CT had an accuracy (mean error) and precision (SD error) of -0.013 ± 0.167 mm (R^2 coefficient of determination of 0.84). CT-based measurement errors for rib cross-sectional geometry were $-0.1 \pm 13.1\%$ (cortical bone cross-sectional area) and $4.7 \pm 1.8\%$ (total cross-sectional area). Rib cortical bone thickness maps show the expected regional variation across a typical rib's surface. The local mid-rib maxima in cortical thickness along the pleural rib aspect ranged from range 0.9 to 2.6 mm across the study population with an average map maximum of 1.4 mm. Along the cutaneous aspect, rib cortical bone thickness ranged from 0.7 to 1.9 mm with an average map thickness of 0.9 mm. Average cross-sectional properties show a steady reduction in total cortical bone area from 10% along the rib's length through to the sternal end, whereas overall cross-sectional area remains relatively constant along the majority of the rib's length before rising steeply towards the sternal end. On average, male ribs contained more cortical bone within a given cross-section than was seen for female ribs. Importantly, however, this difference was driven by male ribs having larger overall cross-sectional areas, rather than by sex differences in the bone thickness observed at specific local cortex sites. The cortical bone thickness results here can be used directly to improve the accuracy of current human body and rib models. Furthermore, the measurement corridors obtained from adult subjects across a wide age range can be used to validate future measurements from more widely available image sources such as clinical CT where gold standard reference measures (e.g. such as direct measurements obtained from cut sections) are otherwise unobtainable.

Key words: computational models; computed tomography; cortical bone; cortical thickness; cross-sectional geometry; rib.

Introduction

Ribs provide crucial protection for the thoracic viscera but are often fractured in a variety of scenarios (Wuermser et al. 2011). In motor vehicle crashes specifically, rib fractures continue to be prevalent despite advances to safety systems and

vehicles. Furthermore, the presence of rib fractures increases mortality and morbidity rates in vulnerable populations (e.g. the elderly) (Sirmali et al. 2003; Stawicki et al. 2004). Recent research has highlighted the need for in-depth exploration of rib geometry to better understand whole thoracic response to loading (Murach et al. 2018) and therefore develop injury mitigation techniques. Broadly, this can be accomplished using computational human body models (HBMs), an important modern tool for injury assessment.

These models rely on accurate input for their prediction of a rib's response to loading. Global and cross-sectional geometry have been identified as important predictors of this response in ribs (Stein, 1976; Agnew et al. 2013, 2018; Holcombe et al. 2016; Murach et al. 2017). Rib cortical bone

Correspondence

Sven A. Holcombe, Morphomics Analysis Group, University of Michigan International Center for Automotive Medicine, 3415 Med Sci I, 1150 W. Medical Center Dr, Ann Arbor, MI, 48105, USA. E: sven-ho@umich.edu

Accepted for publication 27 May 2019

Article published online 21 June 2019

thickness spans approximately 0.1–2.4 mm (Mohr et al. 2007; Choi & Kwak, 2011; Agnew et al. 2018) and is commonly represented in finite element (FE) computational models using shell elements surrounding a solid trabecular core. Li et al. (2010) found that models which incorporate variable thickness into their cortical bone definitions can better predict a rib's structural response. However, the precise distribution of thicknesses along and around rib bones is not well understood. Current sources report thickness values only in aggregation across particular zones around the rib's circumference or along its length (Mohr et al. 2007; Mayeur et al. 2010; Agnew et al. 2018). In most current models the rib global geometry is drawn from a single individual, and cortical bone thickness values are drawn from these limited or simplified literature sources (Kemper et al. 2007; Choi et al. 2009; Gayzik et al. 2011). Furthermore, there is now evidence that cross-sectional bone area and bone distribution may contribute more than just cortical thickness in predicting rib structural properties (Agnew et al. 2018), highlighting the need to quantify all rib cross-sectional geometry more thoroughly across the population. Despite the current knowledge that precise rib cross-geometry is crucial for predicting rib fracture properties, the incorporation of such geometry at the level of detail necessary to reflect true human variation has not been fully realized in current HBMs. When rib modifications are made to HBMs to simulate population-based differences, a greater emphasis is generally placed on altering material properties and gross thoracic geometry than on cross-sectional rib geometry to achieve the desired structural results (Ito et al. 2009; Schoell et al. 2015).

The Cortical Bone Mapping (CBM) methodology allows for accurate measurements of these important geometric factors from CT imaging (Treece et al. 2010; Treece & Gee, 2015; Holcombe et al. 2018). CBM has been previously applied to ribs for tracking bone thickness reductions after cancer therapy (Okoukoni et al. 2016), but it has not yet been used to report rib cortical bone thickness distributions from individuals or across populations.

In this study we apply the CBM method to high resolution CT scans of full ribs. We assess the accuracy of this method against cross-sectional histology images taken at key locations along each rib and develop full cortical bone thickness maps along and around individual ribs. We spatially register these maps from multiple individuals to present a detailed average thickness map that is representative of an American adult population. The methodology presented here can be used to build individualized rib models, while the aggregated maps can be applied to enhance general population models.

Materials and methods

This study utilizes histology images extracted from, and CT image data covering, 33 complete sixth-level ribs ethically obtained from

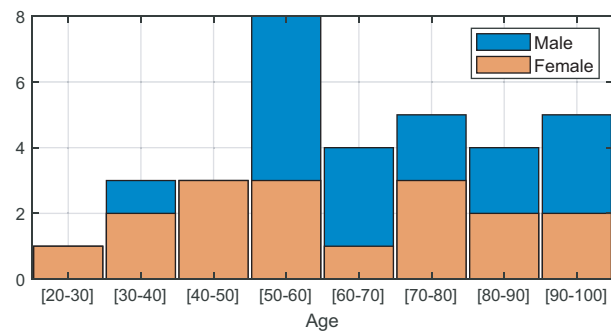


Fig. 1 Stacked subject age counts by sex and decade of life.

anatomical donors in Ohio, USA (16 male, 17 female) with no existing trauma or gross pathological condition affecting the ribs. Subject ages ranged from 24 to 99 years (average \pm SD 65 ± 21) with distributions shown by sex in Fig. 1. Male subjects (70 ± 18 years) were on average older than female subjects (60 ± 22 years); however, this difference was not statistically significant ($P = 0.15$).

Complete ribs were excised from subjects soon after death, and subsequently CT scans of each rib wrapped in saline-soaked gauze were taken using a Phillips Vereos digital PET/CT with 64-slice Ingenuity technology at an axial resolution of 0.15 mm per pixel with slice spacing of 0.67 mm per pixel (i.e. $0.15 \times 0.15 \times 0.67$ mm voxels). Ribs were oriented with their end-to-end axis aligned vertically in the scan such that mid-rib regions were approximately co-planar with the scan's axial plane. After experimental bending tests, cross-sections perpendicular to the long axis of the rib were taken immediately adjacent to each fracture site (39 total sites at either one or two fracture sites per rib) while ensuring no disruption to the bone cortex. Approximate fracture site locations – measured manually using string – were noted as a percentage of rib curvilinear length. Slides were then prepared according to undecalcified hard tissue histology standards (see Agnew et al. 2018). High-resolution microscopy (Olympus BX61VS) allowed for direct image capture (i.e. no reconstruction) of the entire rib section at $100\times$ total magnification and a resolution of 0.69 microns per pixel.

Histology image processing

Periosteal and endosteal cortical borders were semi-manually identified on each histology image using IMAGEJ software (NIH) by an experienced bone histologist (A.A.) (Dominguez & Agnew, 2019). These were used as gold standard cortical bone cross-sectional geometries at their specific rib locations, and each histology image was spatially registered within its corresponding CT image volume as follows. First, rigid registration errors were calculated between the histology-derived periosteal border and those taken from successive cross-sectional cuts through an initial CT-derived periosteal surface (described below). Local minima in registration error indicated strongly matching regions, and visual overlays of the histology image onto the CT volume were used for minor adjustment to align cortices and trabeculae between the two modalities. A typical overlay is presented in Fig. 2 showing the local patterns of trabecular bone – clearly visible on histology and slightly blurred on CT – in strong alignment. For all cut histology sections, the location in CT image space (along the rib's length) of minimum rigid registration error occurred near to the corresponding physical fracture location that was noted by hand. In all cases the final chosen position that showed the strongest coherence in trabecular patterns between

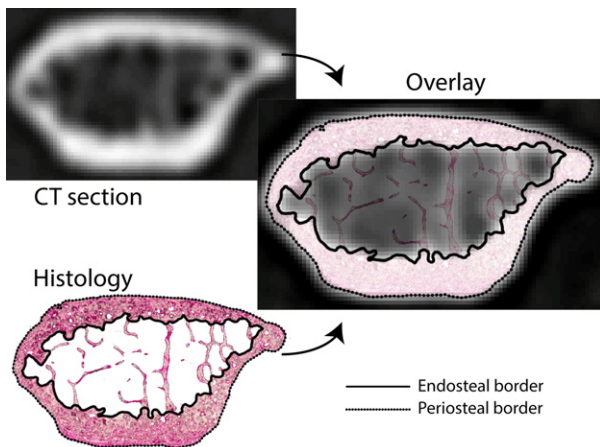


Fig. 2 Exemplar histology image overlay showing the spatial correspondence to the underlying CT image volume at each chosen cross-sectional position.

histology and CT was $< 1\%$ in rib length from the position exhibiting minimum rigid registration error.

CT image processing

An initial and approximate 3D periosteal surface was generated from each rib's CT volume via segmentation performed in MIMICS (v19, Materialise). All subsequent image and statistical analyses were performed in MATLAB (The Mathworks). A central axis along the rib was formed from the rib head (at the vertebral or posterior end) to its sternal (or anterior) end by fitting a smoothed spline through the 2D centroids obtained from successive cross-sectional cuts across this initial periosteal surface. This initial surface was then discretized along the central axis into 301 successive and equally spaced cross-sections. Each section was further discretized into 80 locations around its circumference to produce an overall surface map as depicted in Fig. 3.

Local pleural and cutaneous aspects for each cross-section were calculated using the two points on its circumference intersected by that section's minor inertial axis. A smoothed spline fitted to these points formed overall rib pleural and cutaneous aspects. Co-alignment between rib surface maps was achieved by aligning the circumferential locations along these aspects.

At each surface location (that is, at 301×80 locations per rib), a 1D cortical signal of the image intensity across the cortex was produced by re-sampling the underlying CT image in a direction normal to the 3D surface at that location. The CBM method (CBM) was then applied to each cortical signal. CBM uses nonlinear optimization to match a model consisting of three constant density regions (y_0 outside the periosteal border, y_1 within the cortex, and y_2 inside the endosteal border) to the cortical signal. The distance between the optimally fitted periosteal and endosteal estimates (x_0 and x_1) provides the local cortical bone thickness, and the collection of individual estimates across a rib's gridded surface provide overall rib thickness maps. As per previous work (Holcombe et al. 2018; Treece et al. 2010) the cortical density model parameter (y_1) was fixed within each CBM optimization to a Hounsfield unit value corresponding to the density seen in the thickest bone region along the rib, and weighting was applied to penalize more aggressively the model fitting errors located near the initial periosteal surface.

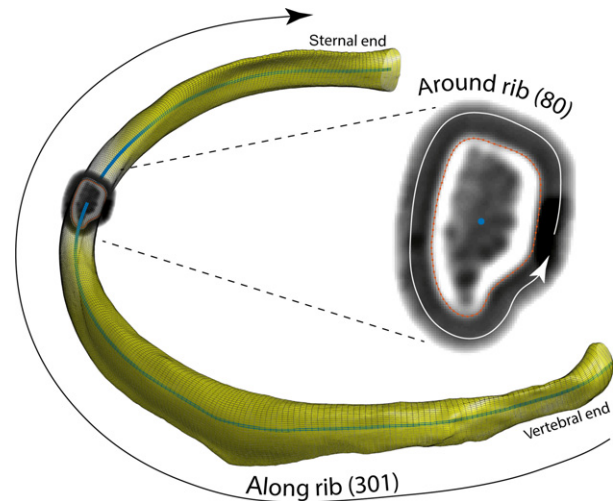


Fig. 3 Ribs are discretized to a 301 (along) by 80 (around) grid of rib surface locations.

In this study, additional error-based local smoothing was applied to the collected x_0 and x_1 value maps using a 0.3-mm Gaussian-shaped smoothing kernel that was further scaled by the inverse of the CBM model fitting error at those same locations. This step served to reduce high-frequency noise in resulting border locations across the rib surfaces and also reduced the influence of poorly fitted individual cortical signals.

Finally, filters were used to suppress potentially misleading thickness measurements within a given cross-section as described in Holcombe et al. (2018) and summarized below. First, individual signals wherein the parameters from the CBM method's optimization step did not converge with internal (non-boundary) values were ignored. Secondly, morphological criteria applied to each circumferential ring of estimated endosteal borders were used to discard signals which did not pass through a single isolated cortical wall. This is most commonly seen near areas of high local curvature such as the costal groove.

Geometric measurements

Overall, the steps above served to produce an underlying 301×80 map of local cortical bone thickness (Ct.Th) estimates obtained from CT, with one map for each of the 33 whole ribs. These maps were averaged to produce an average Ct.Th map for the study population.

Additionally, the sequence of periosteal and endosteal border positions around each individual cross-section were joined to produce the geometric shape of that section's predicted cortical shell (for 301 shells per rib). Cross-sectional geometry measurements of each of these shells were calculated, consisting of the total sub-periosteal area (Tt.Ar), the cortical area (Ct.Ar), the endosteal area (Es.Ar), and the cortical shell's maximal (or principal) and minimal (or secondary) area inertial moments (I_{MAX} and I_{MIN}). The I_{MAX} and I_{MIN} inertial axes intersect the 2D centroid of the cortical shell and, with rib cross-sections generally elongated, the I_{MAX} inertial axis occurs along an approximately inferior to superior aspect, while the I_{MIN} inertial axis lies perpendicular to I_{MAX} along a pleural to cutaneous aspect. As a descriptor of rib cross-sectional aspect ratio, I_{RAT} was calculated as I_{MAX} divided by I_{MIN} . The six overall cross-sectional measurements were grouped by position along a rib to report population average values and a $\pm 1SD$ population corridor, each calculated as a function of position from the vertebral rib end to the sternal rib end.

Regional sex-based differences in bone thickness and in cross-sectional geometry measurement distributions were assessed via two-sample *t*-tests with significance determined at the $P < 0.05$ level.

Validation against histology

Each histological image ($n = 39$) matched a specific cross-sectional position along the length of one of the 33 whole ribs. A CT validation set was produced by using gold standard measurements obtained directly from the periosteal and endosteal borders drawn on the histology images, and pairing them with measurements from the spatially equivalent locations within the full CT image volumes of the same ribs. Therefore, the validation set for all CT measurements consisted of 3120 local cortical bone thickness (Ct.Th) measurement pairs (at 80 locations around each of 39 sections), and 39 pairs (one per histology image section) for the Tt.Ar, Ct.Ar, Es.Ar, I_{MAX}, I_{MIN}, and I_{RAT} rib cross-sectional shape measurements. Additionally, the difference in principal inertial axis orientation (I_{ANG}) between the cortical shell shapes obtained using CT and histology was calculated. For I_{ANG}, a positive difference indicated rotational misalignment (having the superior rib aspect rotate towards the pleural side) of the cortical shell obtained using CT compared with the target cortical shell from histology.

Individual thickness values discarded via the morphological filters described above were excluded from the Ct.Th validation set, and their border positions were linearly interpolated via neighboring successful measurements to provide complete cross-sectional geometry. For all measurement pairs in the validation set, the measurement accuracy (mean error) and precision (SD error) of CT-based predictions was calculated.

Results

Accuracy assessment

From 3120 histology-matched cortical bone signal locations (at 80 locations sampled around each of the 39 sections with histology), 37 signals did not converge adequately during CBM optimization and 161 were identified by morphological filters as not falling across a clear singular cortex. The remaining 2922 (94%) predictions of Ct.Th from CT for comparison with gold standard values from their histology-based pairs, are shown as scattered data in Fig. 4.

Overall accuracy (mean error) and precision (SD error) of predicted cortical thickness values from CT ($n = 2922$) was -0.013 ± 0.167 mm. Table 1 also lists the accuracy and precision for CT-based predictions of each of the full cross-sectional property measurements ($n = 39$). In general, cross-sectional property predictions were well correlated with gold standard values ($R^2 > 0.91$ for all properties), but with CT-based predictions on average overestimating area properties by 0.1% (Ct.Ar), 4.7% (Tt.Ar), and 6.8% (Es.Ar).

Sectional property variation

Average values and 1SD male and female corridors for regional Ct.Ar, Tt.Ar, Es.Ar, I_{MAX}, I_{MIN}, and I_{RAT} are shown in Fig. 5, and all corridor data is included as Data S1.

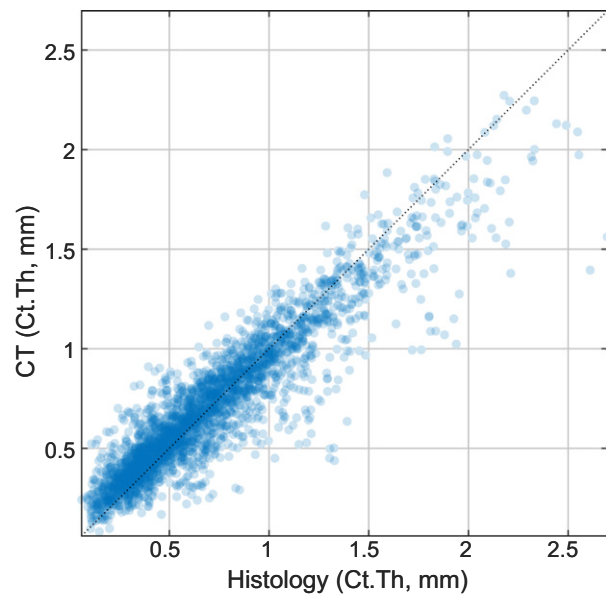


Fig. 4 Predicted individual thickness measurements compared to spatially equivalent measures from histology (coefficient of determination $R^2 = 0.84$, $P < 0.0001$).

Specifically, male ribs had significantly larger (at the $P < 0.05$ level) Ct.Ar at 56% of rib locations, and significantly larger Tt.Ar, Es.Ar, Es.Ar, I_{MAX}, and I_{MIN} at over 96% of rib locations. Inertial aspect ratio (I_{RAT}) varied along the rib, with local peaks in aspect ratio occurring near either rib end and within a region spanning approximately 25–50% of the rib's length. This region corresponds to the greatest

Table 1 Values from gold standard histology and their predictions errors from CT (mean \pm SD) for Ct.Th ($n = 2922$) and whole rib section properties ($n = 39$), with coefficients of determination (R^2) from linear regression ($P < 0.0001$ for all models)

Measure	Histology Mean \pm SD	CT		
		Mean \pm SD	Pred. error	R^2
Ct.Th (mm)	0.7 \pm 0.4	0.7 \pm 0.3	-0.013 ± 0.167	0.84
Ct.Ar (mm ²)	20.4 \pm 8.0	20.4 \pm 6.3	0.03 \pm 2.67	0.91
Tt.Ar (mm ²)	64.1 \pm 20.8	67.1 \pm 21.5	3.00 \pm 1.16	1.00
Es.Ar (mm ²)	43.7 \pm 17.1	46.7 \pm 18.2	2.97 \pm 2.54	0.98
I _{MAX} (mm ⁴)	247.5 \pm 160.3	262.8 \pm 151.6	15.34 \pm 42.69	0.93
I _{MIN} (mm ⁴)	124.0 \pm 86.5	132.7 \pm 82.8	8.61 \pm 14.44	0.97
I _{RAT}	2.2 \pm 0.9	2.2 \pm 0.9	-0.04 ± 0.14	0.98
I _{ANG} (deg.)			0.63 \pm 2.45	

prominence of the rib's costal groove, and here female ribs were significantly more elongated than male ribs, whereas rib aspect ratios in other regions were not significantly different. As seen on Fig. 5, the maximal CT_{AR} along the length of the rib occurs near the rib tubercle (approximately 10% rib length) and decreases steadily towards the sternal end, whereas Tt_{AR} remains relatively constant across most of a rib's length before increasing sharply towards its sternal end. These cross-sectional changes along a rib's length are visualized in Fig. 6, which shows the CT predictions of cortical bone borders for a number of subjects and rib locations, and highlights the overall inter-subject and intra-subject variability in rib cross-sectional geometry.

Cortical bone thickness maps

The full rib cortical bone thickness map (CT_{TH}) was calculated for each rib, and the resulting average CT_{TH} map from the full sample is shown in Fig. 7. Adding all rib locations together, males and females had average \pm SD CT_{TH} values of 0.71 ± 0.35 mm and 0.76 ± 0.38 mm, respectively. Assessed on a regional basis, the majority (90.4%) of rib surface locations did not show a significant difference ($P > 0.05$) in cortex thickness between males and females. Therefore, CT_{TH} thickness maps have been shown using pooled data from both sexes. This pooled CT_{TH} map alongside separated male and female average maps are provided as Data S1.

Discussion

Here we have assessed detailed rib cortical bone thickness and cross-sectional geometry from 33 adult sixth ribs. Starting with an initial approximate rib segmentation, the CBM method was applied using error-weighted smoothing and morphological filters, and average cortical bone thickness maps and cross-sectional property 1SD corridors for males and females have been presented.

The measurement techniques used in this study are similar to those presented in Holcombe et al. (2018) with adjustments to allow for full rib image volumes rather than individual rib section images. The image volumes in the current study have $0.15 \times 0.15 \times 0.67$ mm voxels, providing resolutions that are both higher (in-plane directions) and lower (out-of-plane direction) than the highest resolution images of 0.37 mm per pixel used in Holcombe et al. (2018). Correspondingly, the current accuracy and precision of measurement predictions from CT are largely similar to those from that previous study, which found prediction errors of -0.03 ± 0.17 mm for CT_{TH} , -0.6 ± 1.5 mm² for CT_{AR} , and 2.1 ± 1.5 mm² for Tt_{AR} .

For measuring cross-sectional rib properties using CT, the current CBM-based methodology is more accurate than traditional CT thresholding methods, which often overestimate the amount of bone in a given cross-section. Perz

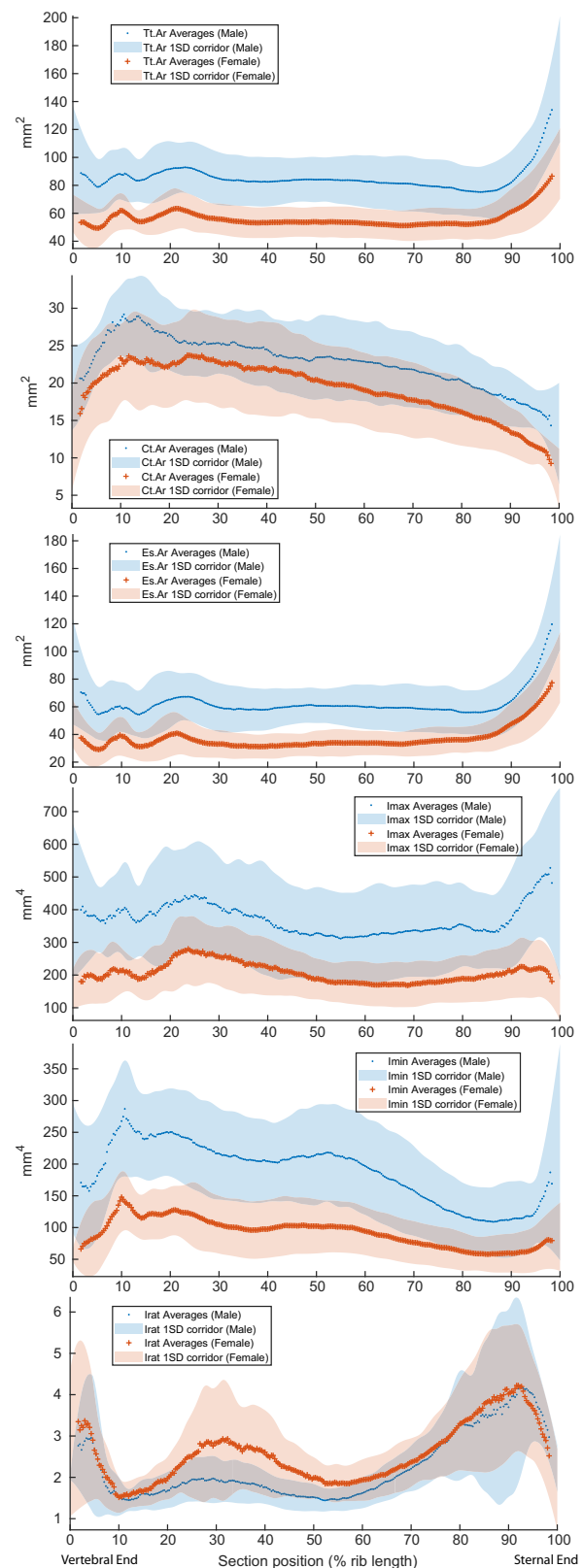


Fig. 5 Measurements by sex of rib cross-sectional total area (Tt_{AR}), cortical bone area (Ct_{AR}), endosteal area (Es_{AR}), primary and second inertial moments ($Imax$, $Imin$) and $Imax/Imin$ inertial moment ratio ($Irat$) as a function of cross-section location from the vertebral (0%) to sternal (100%) rib ends.

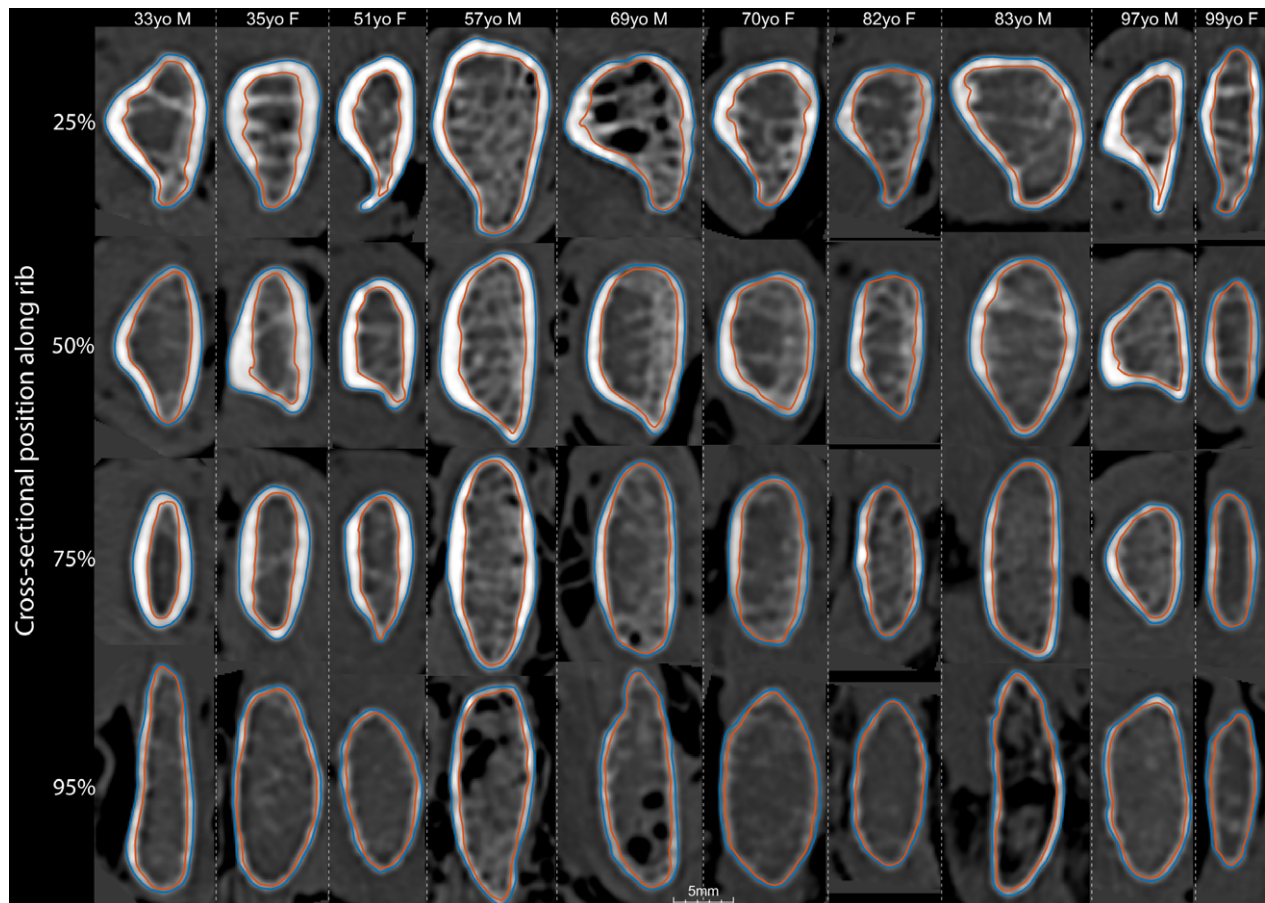


Fig. 6 Exemplar cross-sections through CT volumes showing the predicted periosteal (outer) and endosteal (inner) cortical border using a range of male and female subjects (see upper labels) and rib locations (see left labels).

et al. (2015) found that simple histogram-based thresholding of CT images resulted in average errors in $T_{T.AR}$ of $8 \pm 3\%$. Murach et al. (2017) used an adaptive histogram-based thresholding technique on 19 CT images of similar resolution to the current study, finding $T_{T.AR}$ errors of $3 \pm 11\%$. Those same studies reported that their CT thresholding techniques produced unacceptable $C_{T.AR}$ overestimations of $40 \pm 12\%$ and $71 \pm 45\%$, respectively. In the current study we see similar or improved accuracy and precision in $T_{T.AR}$ with errors of $4.7 \pm 1.8\%$, and greatly reduced errors of $0.1 \pm 13.1\%$ for $C_{T.AR}$. It is informative to note that the initial periosteal border in the current study – obtained using a standard 226 HU threshold for bone segmentation – also overestimated $T_{T.AR}$ on these same images by $21 \pm 4\%$.

Sex-based sectional differences

Results highlighted in Fig. 5 show that while there are similar trends in average rib cross-sectional properties along the lengths of male and female ribs, there were significant sex-based differences in their magnitudes, with male ribs being

larger in terms of all area and inertial measurements and at a large majority of positions along those ribs. Comparing results for $C_{T.TH}$, on the other hand, sex-based differences were less pronounced, with male ribs having significantly thicker cortices at just 2.1% of rib surface locations (at the $P < 0.05$ level) and female ribs having thicker cortices at 7.5% of rib surface locations. Taken together, these results indicate that the larger $C_{T.AR}$ seen in males is primarily due to males having larger overall cross-sectional size to their ribs than females, rather than males having rib bones with thicker cortices than females. Notably, also, female subjects in this study were on average older (although not significantly older) than the males, and bone quantity in general is known to decrease with age. However, (Agnew et al. 2018) found no significant decrease in average pleural or cutaneous $C_{T.TH}$ with age (or by sex) on a large sample of ribs, suggesting age is likely not a confounding factor here.

As seen in Fig. 5, the rib cross-sectional position of highest $C_{T.AR}$ is near the rib tubercle (approximately 10% rib length), and a steady reduction in $C_{T.AR}$ is seen from this location towards the sternal end. Rib $T_{T.AR}$, however, remains relatively constant across most of a rib's length

before increasing sharply towards its sternal end, despite variability in the qualitative shape seen in Fig 6. Each of these observations match findings by Choi & Kwak (2011) who measured cross-sectional areas from ribs of seven elderly male cadaveric ribs. While not reporting sixth rib data, their fifth rib results showed an average $T_{T.AR}$ of 91 mm^2 that was constant from the tubercle to 90% of the rib's length, and a drop in $C_{T.AR}$ across that same region from 26 to 19 mm^2 . Each of these fall within the 1 SD male corridors obtained from the current study.

Cortical bone thickness map

Consistent patterns in cortical bone thickness maps were also seen across individuals, as typified by the population average map (Fig. 7). Beyond the tubercle, all ribs showed local $C_{T.TH}$ maxima along the pleural and cutaneous aspects and local $C_{T.TH}$ minima along the superior and inferior aspects, with these features lessening at the most sternal end of the rib to form uniformly thin cortices like those seen at the 95th percentile position in Fig. 6. The pleural aspect contained the thickest regions of bone, with $C_{T.TH}$ values peaking at between 0.9 and 2.6 mm across the population at approximately mid-rib locations.

Thickness map registration

When performing statistical aggregation it is important that variable sets (in this case individual thickness maps) are spatially registered to maintain correspondence between regions on the maps from different individuals. The one-dimensional registration along the length of the rib is straightforward, whereby sample locations are equally spaced along the rib's central axis from the vertebral to sternal rib ends. In this study the further registration of rotational positions around the ribs is based only on the surface geometry of the ribs. We have taken the general approach of positioning the pleural and cutaneous registration aspects at locations where the rib section's secondary inertial axis intersects with its periosteal border. For continuity, these locations were calculated at each cross-section and a smoothing spline was fitted to provide their exact location.

Having registration depend only on rib surface geometry means that local features of the thickness maps themselves (which are a product of external and internal surface geometries) are not explicitly aligned. For example, all ribs in this study were seen to have a regional maxima along or near their pleural margin. Yet, these regional maxima did not align precisely to the pleural position as determined by only that rib's surface geometry.

It would be desirable to have the regional maximum from the average thickness map correspond to the average regional maxima from each constituent rib map. In the current study, the average thickness map registered by surface

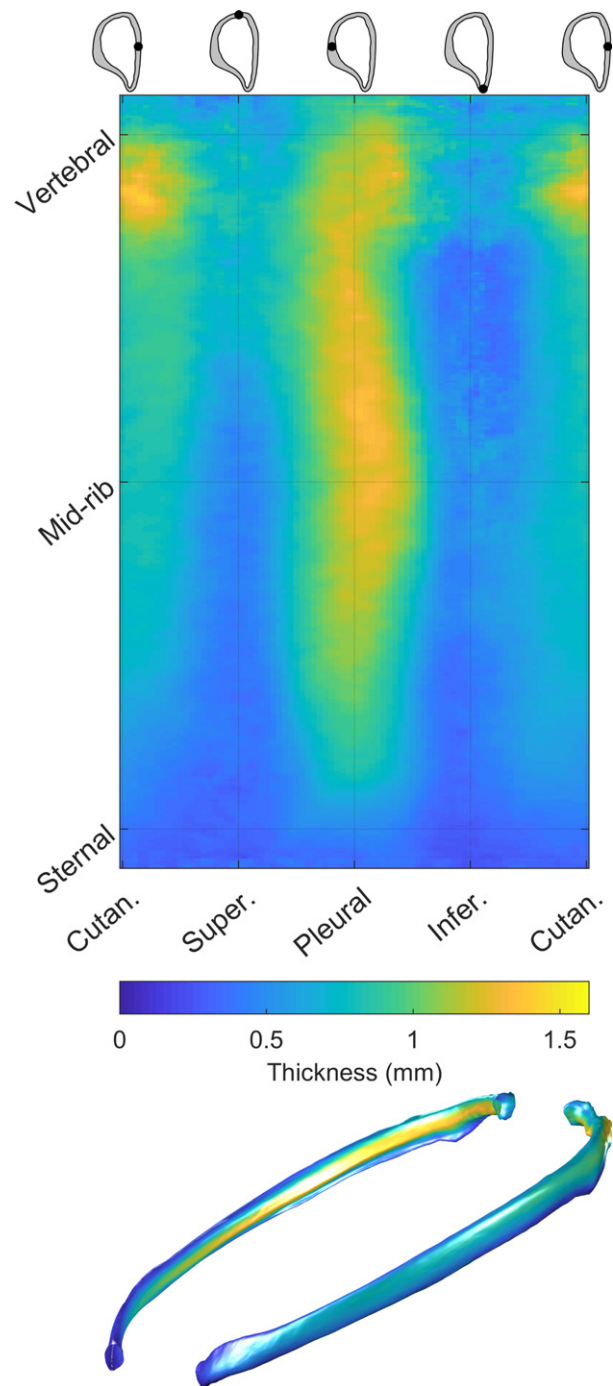


Fig. 7 The average rib cortical bone thickness map in gridded form (above) and projected onto exemplar subject geometry (below).

features alone actually underestimated the average of the regional maxima along the mid-rib pleural aspect by approximately 0.06 mm (5%). Similarly, the regional minima at the superior aspect of the mid-to-sternal portion rib was overestimated by approximately 10% compared with the collection of minima from each individual thickness map.

Limitations

A primary limitation of the current study is that its results are presented only for sixth level ribs. With ribs of different levels in the rib cage serving different mechanical roles, it is expected that both global and local anatomies will differ accordingly. Indeed, ribs do differ by level in terms of global size and shape (Weaver et al. 2014; Wang et al. 2016; Holcombe et al. 2017), overall mechanical stiffness Kindig et al. (2011), and local cross-section (Choi & Kwak, 2011; Wang et al. 2016). Nevertheless, the combination of CT and histological image modalities used in this study allows us to establish methods for validating the typical full-rib properties of this mid-level rib.

This reference at the sixth rib level can be used to verify that future measurements – which may be obtained from sources such as clinical CT scans with less optimal imaging characteristics and without recourse to gold standards for validation – are free of systematic bias due to their particular imaging conditions.

The current study population covered a wide age range with the intention that average results are seen as typical of an adult (US) population. In measures where significant sex-based differences were found, we have chosen to provide male and female results separately. Future work should aim to broaden the subject population to include children, and to increase the subject count so as to allow statistical analyses that incorporate other demographic factors such as age, stature, body mass, and ancestry.

Applications and future work

The technique outlined in this study can be used to create accurate rib endosteal and periosteal surfaces along the entire length of the rib, which can improve simulation efforts greatly. The rib cortical bone thickness reference data used in current HBMs is limited in terms of the population from which it was drawn, and in terms of the geometric detail that it provides. Li et al. (2010) demonstrated the positive effects of including more specific cortical thickness variation into simulation studies, and Agnew et al. (2018) quantified the significant effect that cross-sectional geometry has on ribs' resistance to loading from physical tests. These studies have demonstrated the need for more advanced approaches to understanding human variation in rib properties and differential rib fracture risk between individuals.

Future work can target the improvement of HBMs by incorporating the results obtained here for cortical bone thickness maps into HBM rib definitions. Future efforts can also assess the geometric accuracy of such models, testing their ability to represent their target population by comparing their modeled rib geometries with the typical adult corridors published here.

Conclusion

Numerical models are an important tool for understanding and preventing traumatic injuries to the chest, and the ribs form a key structural model component. Models are typically developed using CT image data, but traditional CT segmentation methods have been inadequate for obtaining accurate cortical bone geometry. As such, only simplified cortex data has been applied based on limited available literature from higher resolution sources.

Here we have applied a CBM methodology to whole human ribs, assessed the accuracy of these techniques against gold standard measurements from histology, and presented detailed population-based data for rib cortical bone thickness and for rib cross-sectional properties. The population data presented here for rib cortical bone thickness and cross-sectional area can be used directly to assess and improve the veracity of current FE models of human ribs. Finally, results here can validate future steps towards personalized and population-based geometry of human ribs from more broadly sampled yet less detailed image data such as live-subject clinical CT scans.

Acknowledgements

We are indebted to the anatomical donors and their families whose generous gifts have made this research possible. Additionally, we would like to thank Randee Hunter, Karen Briley, Michael Knopp, and the Wright Center of Innovation in Biomedical Imaging for contributions to CT acquisition, and Victoria Dominguez for contributions to histological preparations and imaging.

Disclosure of interests

The authors report that there are no conflicts of interest which might affect this work.

References

- Agnew AM, Moorhouse K, Kang Y-SS, et al. (2013) The response of pediatric ribs to quasi-static 412 loading: mechanical properties and microstructure. *Ann Biomed Eng* **41**, 2501–2514.
- Agnew AM, Murach MM, Dominguez VM, et al. (2018) Sources of variability in structural bending response of pediatric and adult human ribs in dynamic frontal impacts. *Stapp Car Crash J* **62**, 119–192.
- Choi H-Y, Kwak D-S (2011) Morphologic characteristics of Korean elderly rib. *J Automot Saf Energy* **2**, 122–127.
- Choi HY, Han J, Park Y, et al. (2009) Digital elderly human body modeling. SAE Technical Paper 2009-01-2262. <https://doi.org/10.4271/2009-01-2262>
- Dominguez VM, Agnew AM (2019) The use of roi overlays and a 426 semi-automated method for measuring cortical area in imagej for histological analysis. *Am J Phys Anthropol* **168**, 378–382.

- Gayzik FS, Moreno DP, Geer CP, et al. (2011) Development of a full body CAD dataset for computational modeling: a multi-modality approach. *Ann Biomed Eng* **39**, 2568–2583.
- Holcombe SA, Wang SC, Grotberg JB (2016) The effect of rib shape on stiffness. *Stapp Car Crash J* **60**, 11–24.
- Holcombe SA, Wang SC, Grotberg JB (2017) The effect of age and demographics on rib shape. *J Anat* **231**, 229–247.
- Holcombe SA, Hwang E, Derstine BA, et al. (2018) Measuring rib cortical bone thickness and cross section from CT. *Med Image Anal* **49**, 27–34.
- Ito O, Dokko Y, Ohashi K (2009). Development of adult and elderly FE thorax skeletal models. SAE Technical Paper 2009-01-0381. <https://doi.org/10.4271/2009-01-0381>
- Kemper AR, McNally C, Pullins CA, et al. (2007) The biomechanics of human ribs: material and structural properties from dynamic tension and bending tests. *Stapp Car Crash J* **51**, 235–273.
- Kindig M, Lau AG, Kent RW (2011) Biomechanical response of ribs under quasistatic frontal loading. *Traffic Inj Prev* **12**, 377–387.
- Li Z, Kindig MW, Subit D, et al. (2010) Influence of mesh density, cortical thickness and material properties on human rib fracture prediction. *Med Eng Phys* **32**, 998–1008.
- Mayeur O, Chaari F, Delille R, et al. (2010) A new method to determine rib geometry for a personalised. In Proceedings of International IRCOBI Conference, pp. 235–246.
- Mohr M, Abrams E, Engel C, et al. (2007) Geometry of human ribs pertinent to orthopedic chest-wall reconstruction. *J Biomech* **40**, 1310–1317.
- Murach MM, Kang Y-S, Goldman SD, et al. (2017) Rib geometry explains variation in dynamic structural response: potential implications for frontal impact fracture risk. *Ann Biomed Eng* **45**, 2159–2173.
- Murach MM, Kang Y-S, Bolte JH, et al. (2018) Quantification of skeletal and soft tissue contributions to thoracic response in a dynamic frontal loading scenario. *Stapp Car Crash J*, **62**, 193–269.
- Okoukoni C, Lynch SK, McTyre ER, et al. (2016) A cortical thickness and radiation dose mapping approach identifies early thinning of ribs after stereotactic body radiation therapy. *Radiother Oncol*, **119**, 449–453.
- Perz R, Toczyski J, Subit D (2015) Variation in the human ribs geometrical properties and mechanical response based on x-ray computed tomography images resolution. *J Mech Behav Biomed Mater* **41**, 292–301.
- Schoell SL, Weaver AA, Vavalle NA, et al. (2015) Age and Sex-Specific thorax finite element model development and simulation. *Traffic Inj Prev* **16**, S57–S65.
- Sirmali M, Türüt H, Topçu S, et al. (2003) A comprehensive analysis of traumatic rib fractures: morbidity, mortality and management. *Eur J Cardiothorac Surg* **24**, 133–138.
- Stawicki SP, Grossman MD, Hoey BA, et al. (2004) Rib fractures in the elderly: a marker of injury severity. *J Am Geriatr Soc* **52**, 805–808.
- Stein ID (1976) Rib structure and bending strength: an autopsy study. *Calcif Tissue Res* **20**, 61–73.
- Treece GM, Gee AH (2015) Independent measurement of femoral cortical thickness and cortical bone density using clinical CT. *Med Image Anal* **20**, 249–264.
- Treece GM, Gee AH, Mayhew PM, et al. (2010) High resolution cortical bone thickness measurement from clinical CT data. *Med Image Anal* **14**, 276–290.
- Wang Y, Cao L, Bai Z, et al. (2016) A parametric ribcage geometry model accounting for variations among the adult population. *J Biomech* **49**, 2791–2798.
- Weaver AA, Schoell SL, Stitzel JD (2014) Morphometric analysis of variation in the ribs with age and sex. *J Anat*, **225**, 246–261.
- Wuermser L-A, Achenbach SJ, Amin S, et al. (2011). What accounts for rib fractures in older adults? *J Osteoporos*, **2011**, Article ID 457591, 6 pages.

Supporting Information

Additional Supporting Information may be found in the online version of this article:

Data S1. Average cortical bone thickness (Ct.Th) values across female and male sixth rib surfaces, and average cross-sectional geometry properties along rib lengths.